Evidence for a 'trap-and-flip' mechanism in a proton-dependent lipid transporter

Elisabeth Lambert[1†], Ahmad Reza Mehdipour[2†], Alexander Schmidt[3], Gerhard Hummer[2,4], Camilo Perez[1*]

[1]Biozentrum, University of Basel, 4056 Basel, Switzerland

[2]Department of Theoretical Biophysics, Max Planck Institute of Biophysics, 60438 Frankfurt am Main, Germany

[3]Proteomics Core Facility, Biozentrum, University of Basel, Basel, Switzerland

[4]Institute of Biophysics, Goethe University Frankfurt, 60438 Frankfurt am Main, Germany

Abbreviated title: Trap-and-flip mechanism in a proton-dependent flippase

[*]Correspondence should be addressed to C.P. (email: camilo.perez@unibas.ch)

[†] These authors contributed equally to this work

32   **Transport of lipids across membranes is fundamental for diverse biological pathways in cells.**

33   **Multiple ion-coupled transporters participate in lipid translocation, but their mechanisms**

34   **remain largely unknown. Major facilitator superfamily (MFS) lipid transporters play central**

35   **roles in cell wall synthesis, brain development and function, lipids recycling, and cell**

36   **signaling. Recent structures of MFS lipid transporters revealed overlapping architectural**

37   **features pointing towards a common mechanism. Here we used cysteine disulfide trapping,**

38   **molecular dynamics simulations, mutagenesis analysis, and transport assays *in vitro* and *in***

39   ***vivo*, to investigate the mechanism of LtaA, a proton-dependent MFS lipid transporter**

40   **essential for lipoteichoic acids synthesis in the pathogen *Staphylococcus aureus*. We reveal**

41   **that LtaA displays asymmetric lateral openings with distinct functional relevance and that**

42   **cycling through outward- and inward-facing conformations is essential for transport activity.**

43   **We demonstrate that while the entire amphipathic central cavity of LtaA contributes to lipid**

44   **binding, its hydrophilic pocket dictates substrate specificity. We propose that LtaA catalyzes**

45   **lipid translocation by a 'trap-and-flip' mechanism that might be shared among MFS lipid**

46   **transporters.**

47

48   Major facilitator superfamily (MFS) transporters are found in all kingdoms of life and move a

49   large variety of molecules across biological membranes [1-8]. Structural characterization of

50   MFS transporters that participate in the uptake of water-soluble molecules and extrusion of

51   drugs has contributed to a broad understanding of their transport mechanism [4, 8-17].

52   However, multiple reports have attributed alternative functions to MFS transporters, such as

53   translocation of lipids associated with fundamental biological pathways. Some examples

54   include the bacterial lysophospholipid transporter LplT, involved in lipids recycling in Gram-

55   negative bacteria [7, 18]; the human transporter MFSD2A, expressed at the blood-brain- and

56   blood-retinal-barrier, contributing to major uptake of docosahexaenoic acid (DHA) [5, 6, 19-

57   21]; the human transporters Spns2 [22, 23], and MFSD2B [24], which contribute to transport

58   of sphingosine 1-phosphate (S1P) in endothelial cells and erythrocytes; and the gentiobiosyl-

59   diacylglycerol transporter LtaA, involved in cell wall synthesis in *Staphylococcus aureus* [25,

60   26]. However, despite their well described cellular roles, the mechanisms of MFS lipid

61   transporters remain insufficiently understood.

62   We have previously shown that LtaA is a proton-dependent MFS lipid antiporter [26].

63   It contributes to adaptation of *S. aureus* to acidic conditions, common in the skin and

64   nasopharynx of the human host [26-28]. LtaA takes part in the assembly of lipoteichoic acids,

65   phosphate-rich polymers important for control of bacterial cell division, protection from

66   environmental stress, host cell adhesion, antibiotic resistance, biofilm formation, and immune

67   evasion [29-32]. *S. aureus* lipoteichoic acids display a polymer of 1,3-glycerol-phosphate

68   repeat units attached to C-6 of the non-reducing glucosyl of the glycolipid gentiobiosyl-

69   diacylglycerol [31-33]. This glycolipid is synthesized at the cytoplasmic leaflet of the

70   membrane by the glycosyltransferase YpfP, and is translocated to the outer leaflet by the

71   activity of LtaA [25, 26]. The essential role of LtaA in adjusting the pool of glycolipids available

72   at the extracellular side of the membrane, makes this protein a central player for lipoteichoic

73   acids assembly and a potential target for drugs aiming to counteract antimicrobial resistant *S.*

74   *aureus* strains e.g., methicillin-resistance *S. aureus* (MRSA) and vancomycin-resistant *S. aureus*

75   (VRSA) [30].

76   Two different general models of transporter-catalyzed lipid translocation have been

77   proposed in the past [34-42]. A 'trap-and-flip' model, in which the lipid substrate is retrieved

78   from one leaflet of the membrane, enclosed into a central cavity, and then delivered to the

79   other leaflet [40, 43, 44], and a 'credit-card' model that departs from the classical alternating-

80   access model and involves translocation of the lipid head-group across a hydrophilic cleft or

81   cavity in the transport protein, while aliphatic chains remain embedded in the membrane [36-

82   38, 41, 42, 45, 46]. However, it is not known which of these two models describe better the

83   mechanism of MFS lipid transporters. Answering this question is not only important to

84   understand the basis of the processes catalyzed by these proteins, but could also provide a

85   foundation for the design of drugs and/or lipid-linked-bioactive molecules targeting cells or

86   organs expressing pharmacologically relevant proteins from this superfamily.

87   Until now, only the high-resolution structures of outward-facing LtaA and inward-

88   facing MFSD2A have been elucidated [21, 26]. Both transporters displayed the canonical MFS

89   fold of 12 transmembrane (TM) helices and an amphipathic central cavity that has not been

90   observed in any MFS transporter of water-soluble molecules. The similar architectural

91   features observed in the structures of LtaA and MFSD2A indicate common elements in their

92   transport mechanisms and likely among all MFS lipid transporters. Here, we used cysteine

93   disulfide trapping of outward- and inward-facing LtaA, in combination with molecular

94   dynamics simulations, mutagenesis analysis, and transport assays *in vitro* and *in vivo*, and

95   showed that cycling through outward- and inward-facing conformations is essential for LtaA

3

96   activity. We demonstrate that LtaA displays membrane exposed lateral openings with distinct

97   functional relevance and characterized the architecture and biochemical properties of the

98   amphipathic central cavity during alternating-access. Our results indicate that while the

99   hydrophilic pocket of the amphipathic central cavity dictates substrate specificity, the

100   hydrophobic pocket is only relevant for aliphatic chains binding. We describe critical

101   mechanistic elements revealing that LtaA adopts a 'trap-and-flip' mechanism that might be

102   shared among MFS lipid transporters.

103

104   **Results**

105   ***Model of inward-facing LtaA and validation by cysteine cross-linking***

106   To investigate whether LtaA uses a 'trap-and-flip' or a 'credit-card' mechanism, we first

107   aimed to establish a system that allowed us to perform cysteine disulfide trapping of end-

108   point conformations of LtaA during its transport cycle. The architecture of the previously

109   solved structure of LtaA [26], facilitates cysteine disulfide trapping of outward-facing states,

110   whereas there is no structural information to guide trapping of inward-facing states. Thus, we

111   first generated an inward-facing model of LtaA using 'repeat-swap' modeling [47]. Like other

112   transporters from the MFS superfamily, the topology of LtaA consists of two domains, a N-

113   terminal domain (TM1-TM6; domain-1), and a C-terminal domain (TM7-TM12; domain-2),

114   each of which contains two structural repeats with inverted-topology related by a pseudo-

115   rotational two-fold symmetry axis parallel to the plane of the membrane (**Fig. 1A,B**). After

116   swapping the conformations of the inverted repeats observed in the outward-facing structure

117   of LtaA (PDB ID 6S7V) [26, 47], we constructed a large set of models *in silico* that were refined

118   aiming to improve side chains packing, stereochemistry, and modeling scores. The models

119   with the best scores converged to one conformation (**Fig. 1C and Suppl. Table. 1**), which

120   displayed multiple interactions between the extracellular parts of TM1-TM7, TM2-TM11, and

121   TM5-TM8, sealing the entrance to the central cavity (**Fig. 1C**). In contrast, the cytoplasmic

122   regions of helices TM2-TM11, TM5-TM8, and TM4-TM10, lining the entrance to the central

123   cavity from the cytoplasm, are away from each other about 16.0±0.1 Å, 16.0±0.1 Å, and

124   17.6±0.2 Å, respectively (**Fig. 1C**). The helical loop between TM6 and TM7 that connects the

125   N- and C-terminal domains was modeled based on the conformation observed in the outward-

126   facing structure.

127   To validate the inward-facing model, we selected pairs of residues among the

128   extracellular regions for which Cβ-Cβ distances were less than 7 Å, but which present Cβ-Cβ

129   distances of over 12 Å in the outward-facing structure (**Suppl. Fig. 1**). Based on these criteria,

130   we identified the pairs F45-T253, A53-T366, and K166-I250 (**Fig. 2A and Suppl. Fig. 1**),

131   occupying three different positions that provide good coverage of the conformational change

132   predicted by our models. We then introduced cysteine residues at these positions on a starting

133   construct in which the one native cysteine in LtaA was replaced with serine. The cysteine-less

134   LtaA variant effectively performed glycolipid flipping in proteoliposomes (**Suppl. Fig. 2**). The

135   three mutants F45C-T253C, A53C-T366C, and K166C-I250C were then irreversibly crosslinked

136   with N,N'-(o-phenylene)-dimaleimide (o-PDM), which has a spacer arm length of 6 Å.

137   Crosslinked and non-crosslinked LtaA mutants were digested with either trypsin or

138   chymotrypsin, and analyzed by high-resolution liquid chromatography–mass spectrometry

139   (LC–MS) to evaluate the presence of non-crosslinked cysteine containing peptides. The

140   peptides abundance was normalized against an internal reference peptide. We successfully

141   identified non-crosslinked peptides in untreated samples of the three mutants F45C-T253C,

142   A53C-T366C, and K166C-I250C (**Fig. 2A and Suppl. Fig. 3**). The abundance of these peptides

143   was clearly diminished in the crosslinked protein samples (**Fig. 2A**), demonstrating that the

144   selected pairs of residues are in close proximity as predicted in the inward-facing model.

145   As a control, we performed a similar experiment but with pairs of residues that were

146   shown to interact at the cytoplasmic region of the outward-facing structure (**Fig. 2B**). Thus,

147   we introduced cysteine residues at the positions K80-E339 and K141-N276, present at the

148   cytoplasmic ends of TM2-TM11 and TM5-TM8, respectively. Cβ-Cβ distances between these

149   residues are smaller than 7.5 Å in the outward-facing structure, but larger than 12 Å in the

150   inward-facing models (**Suppl. Fig. 1**). LC-MS analysis of the double mutants K80C-E339C and

151   K141C-N276C confirmed the proximity of these residues as non-crosslinked peptides are more

152   abundant in untreated samples, whereas in the presence of the cross-linking agent their

153   abundances decrease substantially (**Fig. 2B**). In summary, our cross-linking analysis support

154   the predicted conformation and interactions reported by the inward-facing model of LtaA and

155   indicate the position of residues to guide cysteine disulfide trapping of LtaA conformations.

156

157

158

Alternating conformations in proteoliposome membranes

159

160   We investigated the conformations displayed by LtaA in membranes by evaluating the

161   cross-linking of double cysteine mutants reconstituted in proteoliposomes (**Fig. 2C**). The

162   cysteine pairs reported on the conformation of the TM helices that line the lateral openings,

163   TM2-TM11 and TM5-TM8 (**Fig. 1C**). We screened for successful cross-links by using a gel-shift

164   assay in which we first incubated with the o-PDM cross-linker, followed by treating the

165   proteoliposomes with 5-kDa PEG-maleimide (mPEG5k) [48]. This treatment generates a

166   substantial shift in the protein mobility in polyacrylamide gel electrophoresis as mPEG5k

167   irreversibly binds free cysteines. However, if the introduced cysteines are cross-linked by o-

168   PDM, then they will not react with mPEG5k and no shift in gel mobility would be observed.

169   We evaluated the cross-linking of residues A53C-T366C (TM2-TM11) and K166C-I250C (TM5-

170   TM8), positioned at the extracellular region, and K80C-E339C (TM2-TM11) and K141C-N276C

171   (TM5-TM8), located at the cytoplasmic region (**Fig. 2C and Suppl. Fig. 4A,B**). Before cross-

172   linking, each double-cysteine mutant showed a gel shift after incubation with mPEG5K, thus

173   demonstrating PEGylation of free cysteines (**Fig. 2C and Suppl. Fig. 4C**), albeit the shift of

174   K166C-I250C is less prominent (**Fig. 2C**). In contrast, after treatment with o-PDM, all the

175   double cysteine mutants were protected from PEGylation, thus showing that all mutants were

176   successfully cross-linked. The cysteine-less control LtaA, did not show a gel shift in any of the

177   conditions (**Fig. 2C and Suppl. Fig. 4C**), demonstrating that the shifts observed for the mutants

178   were due to PEGylation of cysteines. These results support that when embedded in the

179   membrane of proteoliposomes, LtaA can adopt conformations where residues at the lateral

180   openings lined by TM2-TM11 and TM5-TM8 display similar distances to those reported by the

181   outward-facing structure and the inward-facing model.

182

Alternating-access to the central cavity is essential for function

183

184   The cross-linking results described above showed that LtaA can cycle through outward-

185   and inward-facing conformations. However, it is not known whether this is required for

186   function. This is important because some flippases and scramblases use a 'credit card' mode

187   of transport, where exposing a side cleft or a cavity to one side of the membrane is sufficient

188   for catalysis of lipid transport across the membrane [36-38, 41, 49]. To answer whether

189   alternating between inward- and outward-facing conformations is important for LtaA activity,

190   we performed copper chloride catalyzed cross-linking of residues located at the lateral

6

191 openings lined by TM2-TM11 and TM5-TM8, and determined proton-coupled glycolipid

192 transport activity of cross-linked LtaA variants in proteoliposomes (**Fig. 3**). In this assay, the

193 addition of the K^+-selective ionophore valinomycin generates a membrane potential of about

194 -60 mV, which drives proton influx. Acidification of the lumen of proteoliposomes quenches

195 the fluorophore 9-amino-6-chloro-2-methoxyacridine (ACMA) causing a decrease in the

196 fluorescence [26]. The double-cysteine mutants A53C-T366C (TM2-TM11) and K166C-I250C

197 (TM5-TM8) close the extracellular side openings, whereas the mutants K80C-E339C (TM2-

198 TM11) and K141C-N276C (TM5-TM8) close the cytoplasmic openings (**Fig. 3A and Suppl. Fig.**

199 **4A,B**). Our results show that except for K141C-N276C (TM5-TM8), independent cross-linking

200 of the remaining three lateral openings decreases LtaA activity relative to non-cross-linked

201 mutants (**Fig. 3A**).

202 In addition, we aimed to completely close the cytoplasmic or extracellular cavities and

203 test the effect on LtaA activity (**Fig. 3B**). To do this, we constructed the mutant A53C-T366C-

204 K166C-I250C that after cross-linking would close the extracellular pathway, while the mutant

205 K80C-E339C-K141C-N276C would close the cytoplasmic pathway (**Fig. 3B and Suppl. Fig. 4A,B**).

206 Our results show that in contrast to non-cross-linked proteins, both mutants display

207 background quenching levels, similar to that observed for protein-free liposomes, thus,

208 indicating strong inhibition of transport activity (**Fig. 3B**). We confirmed cross-linking of each

209 double- and tetra-cysteine mutant reconstituted in proteoliposomes by gel shift assays after

210 incubation with mPEG5K (**Fig. 3C,D and Suppl. Fig. 4D**), which showed that after treatment

211 with copper chloride, all the mutants were protected from PEGylation, whereas before cross-

212 linking a gel shift was observed. This confirmed that all mutants were successfully cross-linked

213 in the proteoliposomes samples used in the assay.

214 Taking together, these results reveal that alternating opening to both sides of the

215 membrane is a requirement for LtaA function. However, not all lateral openings seem to have

216 the same functional relevance. In particular, our results demonstrate that while both

217 extracellular lateral openings are similarly important for function, the cytoplasmic lateral

218 opening lined by TM2 and TM11 has a more significant role, as revealed by the low activity of

219 the cross-linked variant K80C-E339C. In contrast, cross-linking of the cytoplasmic lateral

220 opening lined by TM5 and TM8, does not seem to affect LtaA function strongly.

221

222

223 ***Dynamics of lateral openings***

224   For lipid transporters that adopt a 'trap-and-flip' mechanism, substrate binding and

225 release involve movement of lipids through lateral openings of the translocation channel [18,

226 21, 40, 43, 44]. We studied the dynamic behavior of the lateral openings in LtaA when the

227 protein is embedded in a lipid bilayer. To do this, we performed molecular dynamics (MD)

228 simulations of outward- and inward-facing LtaA in a membrane composed of POPG (65%),

229 diacylglycerol (20 %), cardiolipin (10 %), and gentiobiosyl-diacylglycerol (5 %), resembling the

230 membrane of *S. aureus* [50]. During the simulations both states were found to be stable as

231 judged by RMSD plots (**Suppl. Fig. 5**). The simulations revealed that all the optimized inward-

232 facing models exhibit a cavity which is open to the cytoplasm and closed to the extracellular

233 space, whereas the cavity of the outward-facing state is open to the extracellular space and

234 closed to the cytoplasm (**Fig. 4A**). In agreement with the observed wider opening of the

235 extracellular lateral openings, the simulations of outward-facing LtaA showed the intrusion of

236 glycolipid and POPG molecules into the putative translocation pathway (**Fig. 4C**). The glycolipid

237 was seen to intrude from the TM5-TM8 opening, with one of the aliphatic tails reaching to the

238 C-terminal hydrophobic pocket, whereas two POPG molecules intrude from the TM2-TM11

239 opening (**Fig. 4C**). By contrast, simulations of inward-facing LtaA did not show lipids entering

240 the cytoplasmic cavity.

241   In the MD simulations of the inward-facing conformation, we found that the

242 cytoplasmic opening between TM2 and TM11 is wider and more dynamic than that between

243 TM5 and TM8 (**Fig. 4B**). The lateral opening between TM2 and TM11 is thus a likely route for

244 entry of glycolipids into the substrate binding site of the transporter. By contrast, in the

245 outward-facing conformation, the two gates have similar widths and dynamics (**Fig. 4B**).

246 Together with the results from the cysteine trapping analysis, this data suggests that both

247 extracellular openings are a likely route for glycolipids exit, whereas the cytoplasmic lateral

248 opening lined by TM2 and TM11 is more relevant for function as it may provide more room

249 for glycolipids to enter the translocation pathway.

250

251 ***The hydrophobic pocket is relevant for lipid transport***

252   Inspection of the central cavity in the *in silico* analysis shows that similarly to what was

253 observed in the outward-facing crystal structure of LtaA [26], the central cavity of the inward-

254 facing state is amphipathic (**Fig. 5A**). The cavity displays a hydrophilic pocket, enclosed mainly

255   by residues from the N-terminal domain (E32, R35, D68, W127 and W150), which we have

256   previously shown to be relevant for recognition of the glycolipid headgroup [26], and a

257   hydrophobic pocket, enclosed mainly by residues from the C-terminal domain (V234, L237,

258   C263, L296, L300, L309, I316, and Y320) (**Fig. 5A**). The recent structure of the MFSD2A

259   transporter trapped in an inward-facing conformation, displays a similar amphipathic central

260   cavity (**Suppl. Fig. 6**) [21]. Computational docking of a glycolipid molecule to inward-facing

261   LtaA suggests that the gentiobiosyl headgroup is preferentially accommodated in the

262   hydrophilic pocket, whereas the diacylglycerol aliphatic tails are docked into the hydrophobic

263   pocket (**Fig. 5B**).

264   A striking feature of the central cavity observed in LtaA and MFSD2A [21], and to our

265   knowledge, not observed in other MFS structures available to date, is the presence of the

266   highly hydrophobic pocket at the C-terminal domains of these transporters (**Fig. 5A and Suppl.**

267   **Fig. 6**). To test the importance of this pocket in LtaA, we have designed mutants that introduce

268   polar residues, thus making it more hydrophilic. We then evaluated growth of *S. aureus*

269   NCTC8325 *ΔltaA* cells complemented with ectopic copies of the *ltaA* gene carrying these

270   mutations (**Fig. 5C and Suppl. Fig 7**). The variants V234T/L237N/I297S, C263S/L309Q/I316N,

271   and Y320R display marked growth defects, whereas the mutant L296D/I316N do not affect

272   growth. Each mutant was also purified and reconstituted into proteoliposomes, followed by

273   determination of their flipping activity (**Fig. 5D**). In agreement with the results from *S. aureus*

274   growth assays, the mutants V234T/L237N/I297S, C263S/L309Q/I316N, and Y320R display low

275   relative activity compared to LtaA-WT (**Fig. 5D**), whereas L296D/I316N display the highest

276   activity among all mutants. In contrast, introducing a mutation that scarcely increases the

277   polarity of the cavity but that changes the size of residues V234 and I316, displayed low

278   relative flipping activity compared to LtaA-WT, but does not affect growth of *S. aureus*

279   NCTC8325 *ΔltaA* cells (**Fig. 5C,D and Suppl. Fig 7**). Taken together, these results support a

280   fundamental role of the hydrophobic pocket in glycolipid transport. As suggested by docking

281   analysis, it is likely that this pocket is involved in binding of the aliphatic tails of the glycolipid

282   substrate. The striking hydrophobicity of the C-terminal TM helices 7, 8, and 10 in multiple

283   MFS lipid transporters (**Suppl. Fig. 8**), and the involvement in coordination of the aliphatic

284   chain of lysophospholipid as revealed by the structure of MFSD2A [21], suggest a shared

285   mechanistic role of the hydrophobic pocket in lipid-tails binding in MFS lipid transporters.

286

The hydrophilic pocket dictates substrate specificity

So far, our results suggest that during transport, LtaA encloses the full glycolipid substrate in the amphipathic cavity. However, understanding the relevance of the individual parts of the substrate molecule, headgroup and aliphatic chains, is fundamental for future design of pharmacologically relevant molecules targeting this and other MFS lipid transporters. To gain insight into whether LtaA displays higher selectivity towards the headgroup than for the diacylglycerol moiety, we performed flipping assays with LtaA-WT co-reconstituted in proteoliposomes together with NBD-labeled Glc_2-DAG (gentiobiosyl-diacylglycerol) and increasing concentrations of Gal_2-DAG (digalactosyl-diacylglycerol) (**Fig. 5E**). Glucose and galactose differ only in the orientation of the -OH group at the C-4 position. Thus, we hypothesized that if the headgroup is more relevant for substrate recognition than the aliphatic chains, then transport of Glc_2-DAG-NBD will be not be affected, since the difference between glucose and galactose would preclude Gal_2-DAG from being a good competitor. On the other hand, if the diacylglycerol moiety is more relevant for substrate recognition, we expect Gal_2-DAG to be a strong competitor, thus, resulting in marked decrease of Glc_2-DAG-NBD transport. Our results show that even under a high excess of Gal_2-DAG, there is no significant effect on Glc_2-DAG-NBD transport (**Fig. 5E**). We have previously shown that gentiobiose (β-D-Glc-(1,6)-D-Glc), a disaccharide with the same composition and conformation as the glycolipid headgroup (Glc_2-DAG), inhibits lipid transport [26]. Taken together, these results suggest that an intact headgroup is highly relevant for substrate binding and transport, and that even small changes to the headgroup abolishes recognition. Independent of the presence of the diacylglycerol moiety and its predicted binding to the hydrophobic pocket, the headgroup seems to dictate whether a glycolipid can be a substrate for LtaA or not.

Discussion

Several transporters of the MFS superfamily have been structurally characterized in one or multiple conformational states [4, 8-17] However, except for the outward-facing structure of LtaA [26], solved by X-ray crystallography, and the inward-facing structure of MFSD2A [21], solved by single particle cryo-electron microscopy, there are no additional structures available of MFS lipid transporters. Despite the differences among their lipid substrates, the distinct composition of bacterial and eukaryotic membranes, and their

10

319   opposite vectorial lipid transport directions, LtaA and MFSD2A share multiple architectural

320   similarities, including a canonical MFS fold of 12 TM helices and an amphipathic central cavity

321   with asymmetric distribution of hydrophobic and hydrophilic residues (**Suppl. Fig. 6**). A similar

322   arrangement of central cavity residues has been predicted to be present in the bacterial

323   lysophospholipid transporter LplT [18], and are likely to be part of the architecture of other

324   MFS lipid transporters (**Suppl. Fig. 8**). These characteristics suggest a common mechanism of

325   substrate recognition and translocation among these proteins. Indeed, LtaA and MFSD2A

326   display strong selectivity towards the headgroup of their lipid substrates [6, 26]. In the case of

327   MFSD2A the zwitterionic charge of the phosphatidylcholine headgroup is fundamental for

328   ligand transport, whereas LtaA displays strong selectivity towards the gentiobiosyl

329   disaccharide headgroup of the glycolipid. Furthermore, LtaA selects against an isomer of the

330   disaccharide headgroup as shown by the poor competition displayed by digalactosyl-

331   diacylglycerol in transport assays (**Fig. 5E**). In contrast, LplT has been shown to exhibit a more

332   relaxed   specificity   towards   the   lipid   headgroup,   being   able   to   transport

333   lysophosphatidylethanolamine and lysophosphatidylglycerol lipids [18].

334   Although MFSD2A and LplT have been shown to strongly select for lysophospholipids,

335   they display relaxed selectivity towards the length of the aliphatic chains [6, 18]. MFSD2A

336   transports docosahexaenoic acid (DHA), an essential omega-3 fatty acid for brain growth and

337   cognitive function, in the form of lysophosphatidylcholine, but can also transport other lipids

338   with at least 14-carbons acyl chain [6]. It is noteworthy that *S. aureus* membranes are rich in

339   diacylglycerols with chains length ranging from C_{15} to C_{18}, with the most dominant lipid species

340   having a $C_{17}:C_{15}$ composition [25]. This variability among diacylglycerols in *S. aureus*, and the

341   measurable translocation of Glc$_2$-DAG-NBD [26], which has a C_{10} acyl chain length and an NBD

342   group linked to one of the diacylglycerol chains, suggest that LtaA displays similar relaxed

343   specificity towards the length of the lipid part.

344   Our results strongly suggest that in contrast to mechanisms proposed for other lipid

345   transporters, LtaA transports gentiobiosyl-diacylglycerol by a 'trap-and-flip' mechanism,

346   which follows the classical alternating-access model of transport [51], with the entire

347   glycolipid entering and leaving the central translocation pathway (**Fig. 5F**). Inward-facing LtaA

348   binds a glycolipid molecule which enters through the lateral opening lined by TM2 and TM11,

349   as suggested by the cross-linking analysis and MD simulations. This triggers a conformational

350   change to an outward-facing state, in which the glycolipid is released into the membrane

11

351   presumably through any of the two extracellular lateral openings. Protonation of residues in

352   the hydrophilic pocket allows transition to the inward-facing conformation, followed by

353   proton release to the cytoplasm.

354   Similar to the asymmetric opening of extracellular and cytoplasmic cavities described

355   here for LtaA, MFSD2A exhibits a wider opening of its cytoplasmic lateral openings [21]. In this

356   case, the extracellular opening is predicted to be narrow due to the constriction imposed by

357   a disulfide bond at the extracellular side of the transporter [21]. Our results suggest that LtaA

358   exhibit wide open extracellular lateral openings, whereas the cytoplasmic openings are

359   narrower. The distinct constrictions of the cavities that recruit the lipid substrate, cytoplasmic

360   cavity in LtaA and extracellular cavity in MFSD2A, might be part of a selectivity filter that

361   confers substrate specificity.

362   In summary, our results provide insights into the molecular mechanism of glycolipid

363   transport by LtaA and support a 'trap-and-flip' model where asymmetrically open lateral

364   'gates' and extracellular and cytoplasmic cavities play an essential role. Our data suggests that

365   the highly selective hydrophilic pocket dictates substrate specificity, but that the hydrophobic

366   pocket is fundamental for aliphatic chains transport. The mechanistic elements described here

367   might be shared by other MFS lipid transporters and can be decisive for the design of drugs

368   targeting these proteins.

369

370   **Methods**

371   **LtaA expression and purification.** The gene encoding *S. aureus* LtaA was cloned into a

372   modified pET-19b vector (Novagen), with an N-terminal His$_{10}$ affinity tag. LtaA WT and

373   mutants were expressed in *E. coli* BL21 Gold (DE3) (Stratagene) cells. Cells were grown in

374   Terrific Broth (TB) medium supplemented with 1% glucose (w/v) at 37ºC. Overexpression was

375   induced with 0.2 mM Isopropyl β-D-1-thiogalactopyranoside (IPTG) for 1h. All following steps

376   were performed at 4 ºC, unless different specified. Cells were harvested by centrifugation,

377   resuspended in 50mM Tris-HCl, pH 8.0; 500mM NaCl; 5mM β-mercaptoethanol; 0.5mM PMSF

378   and disrupted in a M-110L microfluidizer (Microfluidics) at 10000 psi chamber pressure.

379   Membranes were pelleted by ultracentrifugation and solubilized in 50 mM Tris-HCl, pH 8.0;

380   200mM NaCl; 20mM Imidazole; 15% glycerol (v/v); 5mM β-mercaptoethanol; 1% Lauryl

381   Maltose Neopentyl Glycol (w/v) (LMNG, Anatrace); 1% N-dodecyl-β-D-maltopyranoside (w/v)

382   (DDM, Anatrace). After removing debri, the supernatant was loaded onto a pre-equilibrated

383 NiNTA superflow affinity column (Qiagen). The column was washed with 50mM Tris-HCl, pH

384 8.0; 200mM NaCl; 50mM Imidazole; 10% glycerol (v/v); 5mM β-mercaptoethanol; 0.02%

385 LMNG and 0.02% DDM and then further washed with the same buffer only containing 0.02%

386 LMNG. Elution was performed in the same buffer containing 200mM Imidazole. Buffer

387 exchange to buffer 10 mM Tris-HCl pH 8.0; 150mM NaCl; 0.02% LMNG was performed using

388 PD-10 columns (GE Healthcare). Analytical size exclusion chromatography was performed on

389 a Superdex 10/300 GL column (GE Healthcare) in buffer 10 mM Tris-HCl, pH 8.0; 150 mM NaCl;

390 0.02% LMNG. [52]

391

392 **Mutagenesis.** LtaA mutants were generated using overlap Extension-PCR, followed by DpnI

393 digestion for two hours at 37°C, and transformation into *E. coli* DH5α cells. The mutations

394 were confirmed by DNA sequencing (Microsynth). All oligos used for mutagenesis are listed in

395 **Suppl. table 2**.

396

397 **YpfP expression and purification.** The gene encoding *S. aureus* YpfP was cloned into a

398 modified pET-19b vector (Novagen) with an N-terminal His$_{10}$ affinity tag. YpfP was

399 overexpressed in BL-21 Gold (DE3) (Stratagene) cells. Cells were grown in TB medium

400 supplemented with 1% glucose (w/v) at 37 ºC until a cell density of OD$_{600}$ = 3. Subsequently,

401 cells were induced with 0.2 mM IPTG for 16h at 24 ºC. Cells were harvested by centrifugation

402 and resuspended in buffer A (50mM Tris-HCl pH 8.0; 200mM NaCl; 3% glycerol; 3mM β-

403 mercaptoethanol) plus 0.5mM PMSF. Cells were disrupted using a tip sonication. After

404 differential centrifugation, the supernatant containing YpfP was incubated with NiNTA resin

405 and left stirring for 1h at 4 ºC. Washing was performed with buffer A complemented with 50

406 mM imidazole pH 8.0, followed by elution with buffer A complemented with 200 mM

407 imidazole pH8.0. YpfP was desalted in buffer 50 mM Tris-HCl pH 8.0; 200 mM NaCl; 10%

408 glycerol using PD-10 columns (GE healthcare). If required YpfP was concentrated using a

409 Vivaspin 20 30MWCO until 2.4 mg/ml, flash frozen in liquid nitrogen and stored at -80 ºC until

410 further use.

411

412 **Synthesis of NBD-glycolipid and glycolipid.** Synthesis of glycolipd and nitrobenzoxadiazole

413 (NBD)-labelled glycolipid was performed using a modification of the protocol described by

414 Jorasch et al [53] and Kiriukhin et al [54]. A final concentration of 2mM UDP-Glucose (Sigma),

13

415   2mM NBD-decanoyl-2-decanoyl-sn-Glycerol (Cayman), and 1.2mg/ml purified YpfP were

416   incubated together for 16h at 30℃. The reaction product was separated using thin-layer

417   chromatography (TLC) with a silica gel matrix (Sigma) in a solvent mixture consisting of

418   chloroform:methanol:water (65:25:4, vol/vol/vol). Silica containing the NBD-glycolipid was

419   recovered from plates, and the NBD-glycolipid was extracted from the silica by incubation with

420   a solvent mixture of chloroform:methanol (50:50, vol/vol), followed by drying of the anchor-

421   LLD under argon atmosphere, and subsequently resuspension in 20 mM Tris-HCl pH 8.0; 150

422   mM NaCl. NBD-glycolipid was flash frozen in liquid nitrogen, and stored at -80℃ until further

423   use. Reaction products were previously characterized [26]. Non-labelled glycolipid was

424   prepared similarly by incubation of 2mM UDP-Glucose, 2 mM 1,2-dimyristoyl-sn-glycerol

425   (Avanti) and 1.2 mg/ml YpfP for 16h at 30°C.

426

427   **Formation of LtaA proteoliposomes.** LtaA was reconstituted in unilamellar liposomes

428   prepared by extrusion through polycarbonate filters (400 nm pore size) from a 3:1 (w/w)

429   mixture of *E. coli* polar lipids and L-α-phosphatidylcholine (Avanti polar lipids) resuspended in

430   20 mM Tris-HCl pH 8.0; 150mM NaCl and 2mM β-mercaptoethanol. After saturation with DDM

431   (Anatrace), liposomes were mixed with purified LtaA in a 50:1 (w/w) lipids/protein ratio. DDM

432   was removed after incubation with BioBeads (BioRad). Proteoliposomes were centrifugated,

433   washed and resuspended to a final concentration of 20mg/ml lipids; 7.8μM LtaA. The

434   proteoliposomes were flash-frozen in liquid nitrogen and stored at -80°C until further use.

435

436   ***In vitro* flipping assay.** Before performing flipping assays, proteoliposomes were thawed, their

437   resuspension buffer was exchanged to 20 mM MES pH 6.5; 150 mM NaCl, and the product of

438   the NBD-glycolipid synthesis reaction was incorporated by performing freeze/thaw cycles.

439   Proteoliposomes and protein-free liposomes were diluted to a concentration of 2 mg/ml lipids

440   followed by extrusion through polycarbonate filters (400 nm pore size). Proteoliposomes were

441   immediately used for flipping assays. In case of competition assays with

442   digalactosyldiacylglycerol (DGDG). DGDG powder (Avanti) was resuspended in 20 mM Tris-

443   HCl; 150 mM NaCl and incorporated into proteoliposomes during freeze/thaw cycles together

444   with the NBD-glycolipid. Flipping of NBD-glycolipid was assessed by determining the

445   percentage of NBD-fluorescence that is quenched after addition of a 5 mM sodium dithionite

446   (Sigma) after 200 seconds of starting fluorescence recording. 100 seconds before finishing

14

447   data recording, 0.5% Triton X100 was added to permeabilize the liposomes, making all NBD-

448   glycolipid molecules accessible to dithionite reduction. The fluorescence after Triton X100

449   addition was used for baseline calculations. Fluorescence was recorded at 20°C using a Jasco

450   Fluorimeter. The excitation and emission wavelengths were 470 and 535 nm, respectively. For

451   analysis the fluorescence intensity was normalized to F/F_{max}. Relative flipping activities were

452   calculated as follows: relative activity = $100 \times ((F/F_{max})_i - (F/F_{max})_{liposomes}) / ((F/F_{max})_{wt} -$

453    $(F/F_{max})_{liposomes})$, where i corresponds to each respective treatment/mutants, liposomes

454   corresponds to liposomes without protein, wt corresponds to wild type LtaA and F/Fmax

455   values correspond to the normalized fluorescence values at the plateau after addition of

456   sodium dithionite. Curves were plotted using GraphPad Prism 8. Time courses of the

457   dithionite-induced fluorescence decay in liposomes were repeated at least 3 times for each

458   individual experiment.

459

460   **Proton-transport assay**. LtaA proteoliposomes and protein-free liposomes were thawed, and

461   their internal buffer exchanged to 5 mM HEPES pH7.3; 100mM KCl. Glycolipid was

462   incorporated during freeze/thaw cycles followed by extrusion through polycarbonate filters

463   (400 nm pore size). After 90s of sonication, proteoliposomes and protein-free liposomes were

464   diluted 25-fold in buffer containing 5 mM HEPES pH 7.3; 10 mM KCl; 90 mM NaCl; 0.5 µM 9-

465   amino-6-chloro-2-methoxyacridine (ACMA). Fluorescence was recorded using a Jasco

466   Fluorimeter with excitation and emission wavelengths of 410 and 480 nm respectively. When

467   the fluorescence signal was stable, H^+ influx was initiated by establishing a membrane

468   potential by the addition of the potassium ionophore valinomycin (5 nM). Time courses of the

469   proton-transport assay in proteoliposomes were repeated at least 3 times for each individual

470   experiment. Crosslinking was performed before the measurement by addition of 2 mM $CuCl_2$

471   to the proteoliposomes during the buffer exchange and incorporation of glycolipid steps. After

472   1h incubation at RT in the dark, $CuCl_2$ was removed by centrifugation, and proteoliposomes

473   were resuspended in buffer 5 mM HEPES, pH7.3; 100mM KCl.

474

475   **LtaA crosslinking and PEGylation**. LtaA mutants incorporated into proteoliposomes were

476   incubated with 2 mM $CuCl_2$ or N,N'-1,2-phenylenedimaleimide (o-PDM) for 1h at RT in the

477   dark. In case of non-crosslinked samples, proteoliposomes were incubated with a proportional

478   volume of DMSO or buffer. Crosslinkers were removed by centrifugation and washing with

479 buffer. To PEGylate free cysteines, LtaA mutants were incubated for 3h at RT in the presence

480 of 0.5 mM mPEG5K-Maleimide (Sigma) and 0.5% SDS. Proteins were separated on 15%

481 polyacrylamide gels and visualized with QuickBlue Protein stain (Lubio science).

482

483 **Sample preparation for LC-MS analysis.** LtaA mutants were purified as described above, and

484 concentrated to a concentration of 0.6 mg/ml. Purified LtaA was incubated for 1h at RT in the

485 dark in the absence or presence of 2 mM o-PDM. Afterwards, 10 mM β-mercatoethanol was

486 added to quench the crosslinker. 1-2 ug of either crosslinked or non-crosslinked LtaA protein

487 were dissolved in 20 µl digestion buffer (0.02% of LMNG; 1 M urea; 0.1 M

488 ammoniumbicarbonate; 10 mM tris(2-carboxyethyl) phosphine (TCEP); 15 mM

489 chloroacetamide, pH = 8.5), reduced and alkylated for 1h at 37 °C. Proteins were digested by

490 incubation with either sequencing-grade modified trypsin (1/50, w/w; Promega, Madison,

491 Wisconsin), chymotrypsin sequencing grade (1/50, w/w, Sigma-Aldrich) or lys-C (1/100, w/w,

492 Wako) overnight at 37°C. Then, the peptides were cleaned using iST cartridges (PreOmics,

493 Munich) according to the manufacturer instructions. Samples were dried under vacuum and

494 dissolved in 0.1 % formic acid solution at 0.5 pmol/ul. All samples were prepared in triplicates.

495

496 **Label-free targeted PRM-LC-MS analysis of cysteine-containing peptides.** In a first step,

497 parallel reaction-monitoring (PRM) assays [55] were generated for all the peptides of LtaA WT

498 and the peptides of the 5 different LtaA cysteine mutants, for each protease. These peptides

499 include the reference peptide for normalization, that is shared for all mutants. Therefore, the

500 specific peptide sequences were loaded into Skyline (version 20.2.0.343 (https://brendanx-

501 uw1.gs.washington.edu/labkey/project/home/software/Skyline/begin.view) and transitions

502 were predicted using the integrated PROSIT algorithm for double and triple charged

503 precursors. Then, protease and isoform specific isolation mass lists were exported and used

504 to generate specific targeted LC-MS analyses. This analysis was carried as described previously

505 [56]. Chromatographic separation of peptides was carried out using an EASY nano-LC 1000

506 system (Thermo Fisher Scientific), equipped with a heated RP-HPLC column (75 µm x 30 cm)

507 packed in-house with 1.9 µm C18 resin (Reprosil-AQ Pur, Dr. Maisch). Aliquots of 1 pmol total

508 peptides were analyzed per LC-MS/MS run using a linear gradient ranging from 95% solvent A

509 (0.15% formic acid, 2% acetonitrile) and 5% solvent B (98% acetonitrile, 2% water, 0.15%

510 formic acid) to 30% solvent B over 90 minutes at a flow rate of 200 nl/min. Mass spectrometry

511 analysis was performed on a Q-Exactive plus mass spectrometer equipped with a
512 nanoelectrospray ion source (both Thermo Fisher Scientific) using a hybrid DDA (top5)/PRM
513 LC-MS analysis. In detail, each MS1 scan was followed by high-collision-dissociation (HCD) of
514 the precursor masses of the imported isolation list and the 5 most abundant precursor ions
515 with dynamic exclusion for 20 seconds. For each mutant and protease, a specific LC-MS
516 method was generated. Total cycle time was approximately 1 second. For MS1, 3e6 ions were
517 accumulated in the Orbitrap cell over a maximum time of 100 ms and scanned at a resolution
518 of 70,000 FWHM (at 200 m/z). Targeted MS2 scans were acquired at a target setting of 3e6
519 ions, accumulation time of 100 ms and a resolution of 35,000 FWHM (at 200 m/z) and a mass
520 isolation window to 0.4 Th. MS1 triggered MS2 scans were acquired at a target setting of 1e5
521 ions, a resolution of 17,500 FWHM (at 200 m/z) and a mass isolation window of 1.4 Th. Singly
522 charged ions and ions with unassigned charge state were excluded from triggering MS2 events.
523 The normalized collision energy was set to 27% and one microscan was acquired for each
524 spectrum. The acquired raw-files were converted to mgf-file format using MSConvert (v 3.0,
525 proteowizard) and searched using MASCOT (Matrix Science, Version: 2.4.1) against a decoy
526 database containing normal and reverse sequences of the predicted SwissProt entries of
527 *Staphylococcus aureus* (strain NCTC 8325 / PS 47, www.ebi.ac.uk, release date 2020/08/21).
528 The 5 LtaA mutants and commonly observed contaminants (in total 6,574 sequences) were
529 generated using the SequenceReverser tool from the MaxQuant software (Version 1.0.13.13).
530 The search criteria were set as following: full tryptic specificity was required (cleavage after
531 lysine or arginine residues); 3 missed cleavages were allowed; carbamidomethylation (C) was
532 set as fixed modification and oxidation (M) as variable modification. The mass tolerance was
533 set to 10 ppm for precursor ions and 0.02 Da for fragment ions. Then, Scaffold (version
534 Scaffold_4.11.1, Proteome Software Inc., Portland, OR) was used to validate MS/MS based
535 peptide and protein identifications. Peptide identifications were accepted if they could be
536 established at a probability greater than 97.0% by the Scaffold Local FDR algorithm. Protein
537 identifications were accepted if they could be established at a probability higher than 99.0%
538 to achieve an FDR less than 1.0% and contained at least 2 identified peptides. Protein
539 probabilities were assigned by the Protein Prophet algorithm [57]. Proteins that contained
540 similar peptides and could not be differentiated based on MS/MS analysis alone were grouped
541 to satisfy the principles of parsimony. Subsequently, all raw-files were imported into Skyline
542 for protein/peptide quantification. To control for variation in sample amounts, all intensities

543   were normalized against the 4 cysteine-free reference peptides. Only peptides that could be

544   confidently identified by database searching were considered for quantification by PRM using

545   the predicted transitions. Statistical analysis and ratio calculations to compare the relative

546   abundance of the peptides between non-crosslinked and crosslinked peptides were

547   performed in Excel. Histograms and P values were generated using Prism 9.

548

549   **Docking of glycolipid.** A 1,2-dihexadecanoic-3-O-(β-D-glucopyranosyl-1→6-O-β-D-

550   glucopyranosyl-sn-Glycerol molecule was docked to the LtaA inward-facing model with

551   Autodock Vina [58]. The initial glycolipid coordinates were generated from 2D geometry in

552   Phenix (eLBOW) [59]. The stereochemistry was corrected in Phenix (REEL)[59]. Docking was

553   performed over a search space of 50x44x76 $Å^3$ covering the central cavity.

554

555   *S. aureus* **phenotypic complementation assay.** Generation of pLOW-ltaA and of

556   *Staphylococcus aureus* NCTC8325 *ΔltaA* genotype was previously described [26]. pLOW vector

557   was used for construction of *ltaA* complentary strains. Point mutations were generated by

558   extension overlap PCR, and then with restriction-ligation cloning using SalI and NotI cloned

559   into pLOW vector [60]. For cloning purposes *E. coli* IM08B was used[61]. The sequence of the

560   resulting constructs was confirmed by DNA sequencing (Microsynth). After conformation of

561   the correct constructs, pLOW vector carrying *ltaA* WT or point mutations were introduced into

562   *S. aureus* NCTC8325 *ΔltaA* by electrophoresis with erythromycin selection (5µg/ml). *S. aureus*

563   cells were grown in 3 ml of Luria-Bertani (LB) medium at 37 °C with 200 rpm until OD600 of

564   0.3. For complementary strains containing a pLOW vector, a final concentration of 5 µg/ml

565   was added to the medium. For the serial dilutions, 5 µl of the original and its dilutions were

566   spotted on LB agar plates buffered with sodium phosphate at pH 6.4 complemented with 0.1

567   mM IPTG. The plates were incubated overnight at 37 °C. Pictures were taken the next morning.

568

569   **Preparation of *S. aureus* membranes for LC-MS analysis.** *S. aureus* cells were grown in 3 ml

570   LB medium at 37 °C with 200 rpm until OD_{600} of 0.4. For complementary strains containing a

571   pLOW vector, a final concentration of 5 µg/ml and 0.1 mM IPTG were added to the medium.

572   After harvesting the cells were resuspended in 10 mM Tris pH8.0; 1 mM EDTA; 25 µg/ml

573   lysostaphin, and incubated for 0.5h at 37 °C. Cells were further subjected to sonication,

574   followed by collection of membranes by ultracentrifugation. The membranes were

18

575   resuspended in 100 mM Tris-HCl; 5% SDS; 10 mM tris(2-carboxyethyl) phosphine (TCEP).

576   Samples were sonicated for 10 minutes, followed by shaking for 1h at 37 °C with 500 rpm. To

577   reduce and alkylate the disulfides a final concentration of 15 mM iodoacetamide was added,

578   and the samples were incubated for 0.5h in the dark at room temperature. Samples were

579   loaded on S-trap Micro Spin column (Protifi). After washing, on column peptide digestion was

580   performed by addition of trypsin in 50 mM triethylammonium bicarbonate (TEAB) buffer, and

581   incubation of 1h at 47 °C. Digested peptides were collected by passing 50 mM

582   triethylammonium bicarbonate (TEAB) buffer, 0.2 % formic acid (w/v) in distilled water, and

583   0.2 % formic acid (w/v) in 50% acetonitrile (v/v) through the column and dried in a SpeedVac

584   (Labconco). Dried peptides were re-suspended in 0.1% formic acid (w/v) and stored at -20 °C.

585

586   **Targeted PRM LC-MS analysis of LtaA WT and mutants.** As a first step, PRM assays [55] for all

587   possible peptides of LtaA with a length of 6 to 25 amino acids comprising double- and triple-

588   charged precursor ions were created. Five peptides were identified to match the length and

589   charge criteria, leading to ten PRM assays in total. These were used to identify LtaA membrane

590   fractions of wild-type *S. aureus*. The setup of the µRPLC-MC system was previously

591   described[56]. Mass spectrometry analysis was conducted using a Q-Exactive mass

592   spectrometer with a nano-electrospray ion source (both Thermo Fisher Scientifice). Each MS1

593   scan was followed by high-collision-dissociation (HCD) of the ten LtaA precursor ions in PRM

594   mode using a global isolation mass list. By applying strict identification criteria, three peptide

595   ions of LtaA LTNYNTRPVK (2+ and 3+ ion) and MQDSSLNNYANHK (2+) were identified, and

596   these were used for label-free PRM quantification. To control for protein variation between

597   different samples, the total ion chromatography (only comprising peptide with two or more

598   charges) was determined for each sample by label-free quantification using Progenesis QI

599   (version 2.0, Waters) and then used to normalize the samples. The integrated peak areas of

600   the three peptide ions that were quantified by PRM were summed up, and used for LtaA

601   quantification.

602

603   **Modeling of inward-facing conformation**. The inward-facing conformation was modelled

604   under the assumption of inverted repeats [47]. Sequence alignments between the two

605   repeats of each domain of LtaA were performed. We structurally aligned R1D1 (residues 16–

606   105) with R2D1 (residues 109-189), and R1D2 (residues 220-302) with R2D2 (residues 309-

19

607   393) using the structure alignment program TMalign resulting in two pairs of alignments.

608   These two pairs of alignments were then used together to build up the final pair-wise

609   alignment between the LtaA sequence and a template in which the LtaA sequence repeats

610   were rearranged in the order R1D2-R1D1-R2D2-R2D1. The initial sequence alignment was

611   then refined by removing gaps in the transmembrane regions and in the secondary structure

612   elements. Further refinements were made to match the secondary structure as observed in

613   the outward-open crystal structure. In particular, we aimed to maintain the helical regions in

614   the template where possible, subject to the pseudo-symmetry between the two MFS

615   transporter domains. We used this alignment and the X-ray crystal structure of LtaA (PDB

616   entry 6S7V)[26] to construct the inward-facing model templates using Modeller 9v24. In 100

617   templates, the side chain packing of the models were re-built using SCWRL4 model. Next, we

618   selected 7 models with the highest MODELLER score and the best MolProbity [62] profile for

619   further analysis. Then, we repacked the side chains using SCWRL4.0[63] and as a last step the

620   models were energetically minimized after placing them in the lipid bilayer using the Gromacs

621   2019.6 steepest descent algorithm for 5,000 steps [64]. To further validate the quality of the

622   models, we assessed the stereochemistry. Evaluation of the model using MolProbity showed

623   that the final minimized models have reasonable qualities (MolProbity score: 2.00-2.3,

624   Ramachandran favored: 92.1-93.6%, and Ramachandran outliers: 0.8-1.90%) (**Suppl. Table 1**).

625

626   **Molecular dynamics simulations of inward-facing conformation models**. To study their

627   dynamics, each of the optimized inward-facing models was placed in a heterogenous lipid

628   bilayer (POPG (65%), diacylglycerol (20 %), cardiolipin (10 %), and gentiobiosyl-diacylglycerol

629   (5 %)) and then solvated in TIP3P water with 150 mM NaCl. The all-atom CHARMM36m force

630   field was used for lipids, ions, and protein [65-67]. All simulations were performed using

631   GROMACS 2019.6 [64]. The starting systems were energy-minimized for 5,000 steepest

632   descent steps and equilibrated first for 1 ns of MD simulations in a canonical (NVT) ensemble

633   and then for 7.5 ns in an isothermal-isobaric (NPT) ensemble under periodic boundary

634   conditions. The initial restrains on the positions of nonhydrogen protein atoms were 4,000

635    $kJ·mol^{-1}·nm^2$. During equilibration, these restraints were gradually released. Particle-mesh

636   Ewald summation with cubic interpolation and a 0.12-nm grid spacing was used to treat long-

637   range electrostatic interactions [68]. The time step was initially 1 fs, and was then increased

638   to 2 fs during the NPT equilibration. The LINCS algorithm was used to fix all bond lengths [69].

639 Constant temperature was set with a Berendsen thermostat [70], combined with a coupling

640 constant of 1.0 ps. A semi-isotropic Berendsen barostat [70] was used to maintain a pressure

641 of 1 bar. During production runs, the Berendsen thermostat and barostat were replaced by a

642 Nosé–Hoover thermostat [71] and a Parrinello–Rahman barostat [72] The unconstrained

643 production trajectories were analyzed with Visual Molecular Dynamics (VMD) [73] and

644 MDAnalysis package [74, 75]. A simulation of each inward-facing model was performed for

645 150 ns.

646

647 **Molecular dynamics simulations of outward-facing conformation.** The outward-facing

648 structure of LtaA (PDB ID 6S7V) was embedded in a lipid bilayer composed of POPG-DAG-CL-

649 gentiobiosyl-diacylglycerol using CHARMM-GUI [76]. The system was then solvated in TIP3P

650 water with 150 mM NaCl. The all-atom CHARMM36m force field was used for lipids, ions, and

651 protein [65-67]. All simulations were performed using GROMACS 2019.6 [64]. Simulations

652 were performed with similar protocols as described above for inward-facing models. The

653 simulation of the outward-facing structure was performed for 960 ns.

654

655 **References**

656 1.   Wang, S.C., et al., *Expansion of the Major Facilitator Superfamily (MFS) to include novel*
657 *transporters as well as transmembrane-acting enzymes.* Biochimica Et Biophysica Acta-Biomembranes,
658 2020. **1862**(9).
659 2.   Quistgaard, E.M., et al., *Understanding transport by the major facilitator superfamily (MFS):*
660 *structures pave the way.* Nat Rev Mol Cell Biol, 2016. **17**(2): p. 123-32.
661 3.   Reddy, V.S., et al., *The major facilitator superfamily (MFS) revisited.* FEBS J, 2012. **279**(11): p.
662 2022-35.
663 4.   Drew, D., et al., *Structures and General Transport Mechanisms by the Major Facilitator*
664 *Superfamily (MFS).* Chem Rev, 2021. **121**(9): p. 5289-5335.
665 5.   Ben-Zvi, A., et al., *Mfsd2a is critical for the formation and function of the blood-brain barrier.*
666 Nature, 2014. **509**(7501): p. 507-11.
667 6.   Nguyen, L.N., et al., *Mfsd2a is a transporter for the essential omega-3 fatty acid*
668 *docosahexaenoic acid.* Nature, 2014. **509**(7501): p. 503-6.
669 7.   Harvat, E.M., et al., *Lysophospholipid flipping across the Escherichia coli inner membrane*
670 *catalyzed by a transporter (LplT) belonging to the major facilitator superfamily.* J Biol Chem, 2005.
671 **280**(12): p. 12028-34.
672 8.   Abramson, J., et al., *Structure and mechanism of the lactose permease of Escherichia coli.*
673 Science, 2003. **301**(5633): p. 610-5.
674 9.   Debruycker, V., et al., *An embedded lipid in the multidrug transporter LmrP suggests a*
675 *mechanism for polyspecificity.* Nature Structural & Molecular Biology, 2020. **27**(9): p. 829-835.
676 10.   Heng, J., et al., *Substrate-bound structure of the E. coli multidrug resistance transporter MdfA.*
677 Cell Res, 2015. **25**(9): p. 1060-73.
678 11.   Deng, D., et al., *Molecular basis of ligand recognition and transport by glucose transporters.*
679 Nature, 2015. **526**(7573): p. 391-6.

680   12.   Deng, D., et al., *Crystal structure of the human glucose transporter GLUT1.* Nature, 2014.
681   **510**(7503): p. 121-5.
682   13.   Nomura, N., et al., *Structure and mechanism of the mammalian fructose transporter GLUT5.*
683   Nature, 2015. **526**(7573): p. 397-401.
684   14.   Sun, L., et al., *Crystal structure of a bacterial homologue of glucose transporters GLUT1-4.*
685   Nature, 2012. **490**(7420): p. 361-6.
686   15.   Billesbølle, C.B., et al., *Structure of hepcidin-bound ferroportin reveals iron homeostatic*
687   *mechanisms.* Nature, 2020. **586**(7831): p. 807-811.
688   16.   Pan, Y., et al., *Structural basis of ion transport and inhibition in ferroportin.* Nature
689   Communications, 2020. **11**(1): p. 5686.
690   17.   Qureshi, A.A., et al., *The molecular basis for sugar import in malaria parasites.* Nature, 2020.
691   **578**(7794): p. 321-325.
692   18.   Lin, Y., et al., *A dual substrate-accessing mechanism of a major facilitator superfamily protein*
693   *facilitates lysophospholipid flipping across the cell membrane.* J Biol Chem, 2018. **293**(51): p. 19919-
694   19931.
695   19.   Angers, M., et al., *Mfsd2a encodes a novel major facilitator superfamily domain-containing*
696   *protein highly induced in brown adipose tissue during fasting and adaptive thermogenesis.* Biochem J,
697   2008. **416**(3): p. 347-55.
698   20.   Quek, D.Q., et al., *Structural Insights into the Transport Mechanism of the Human Sodium-*
699   *dependent Lysophosphatidylcholine Transporter MFSD2A.* J Biol Chem, 2016. **291**(18): p. 9383-94.
700   21.   Cater, R.J., et al., *Structural basis of omega-3 fatty acid transport across the blood–brain barrier.*
701   Nature, 2021.
702   22.   Kawahara, A., et al., *The sphingolipid transporter spns2 functions in migration of zebrafish*
703   *myocardial precursors.* Science, 2009. **323**(5913): p. 524-7.
704   23.   Zhu, X., et al., *Biological function of SPNS2: From zebrafish to human.* Mol Immunol, 2018. **103**:
705   p. 55-62.
706   24.   Vu, T.M., et al., *Mfsd2b is essential for the sphingosine-1-phosphate export in erythrocytes and*
707   *platelets.* Nature, 2017. **550**(7677): p. 524-528.
708   25.   Grundling, A. and O. Schneewind, *Genes required for glycolipid synthesis and lipoteichoic acid*
709   *anchoring in Staphylococcus aureus.* J Bacteriol, 2007. **189**(6): p. 2521-30.
710   26.   Zhang, B., et al., *Structure of a proton-dependent lipid transporter involved in lipoteichoic acids*
711   *biosynthesis.* Nat Struct Mol Biol, 2020. **27**(6): p. 561-569.
712   27.   Parlet, C.P., M.M. Brown, and A.R. Horswill, *Commensa Staphycocci influence Staphylococcus*
713   *aureus SKin Colorizatin and Disease.* Trends in Microbiology, 2019. **27**(6): p. 497-507.
714   28.   Sakr, A., et al., *Staphylococcus aureus Nasal Colonization: An Update on Mechanisms,*
715   *Epidemiology, Risk Factors, and Subsequent Infections.* Front Microbiol, 2018. **9**: p. 2419.
716   29.   Ahn, K.B., et al., *Lipoteichoic Acid Inhibits Staphylococcus aureus Biofilm Formation.* Front
717   Microbiol, 2018. **9**: p. 327.
718   30.   Hesser, A.R., et al., *The length of lipoteichoic acid polymers controls Staphylococcus aureus cell*
719   *size and envelope integrity.* J Bacteriol, 2020.
720   31.   Xia, G., T. Kohler, and A. Peschel, *The wall teichoic acid and lipoteichoic acid polymers of*
721   *Staphylococcus aureus.* Int J Med Microbiol, 2010. **300**(2-3): p. 148-54.
722   32.   Percy, M.G. and A. Grundling, *Lipoteichoic acid synthesis and function in gram-positive bacteria.*
723   Annu Rev Microbiol, 2014. **68**: p. 81-100.
724   33.   Fischer, W., et al., *Structural Requirements of Lipoteichoic Acid Carrier for Recognition by the*
725   *Poly(Ribitol Phosphate) Polymerase from Staphylococcus-Aureus H - a Study of Various Lipoteichoic*
726   *Acids, Derivatives, and Related-Compounds.* Journal of Biological Chemistry, 1980. **255**(10): p. 4550-
727   4556.
728   34.   Neumann, J., D. Rose-Sperling, and U.A. Hellmich, *Diverse relations between ABC transporters*
729   *and lipids: An overview.* Biochim Biophys Acta Biomembr, 2017. **1859**(4): p. 605-618.

730   35.   Pomorski, T.G. and A.K. Menon, *Lipid somersaults: Uncovering the mechanisms of protein-mediated lipid flipping.* Prog Lipid Res, 2016. **64**: p. 69-84.

732   36.   Perez, C., et al., *Structure and mechanism of an active lipid-linked oligosaccharide flippase.* Nature, 2015. **524**(7566): p. 433-8.

734   37.   Brunner, J.D., et al., *X-ray structure of a calcium-activated TMEM16 lipid scramblase.* Nature, 2014. **516**(7530): p. 207-12.

736   38.   Hiraizumi, M., et al., *Cryo-EM structures capture the transport cycle of the P4-ATPase flippase.* Science, 2019. **365**(6458): p. 1149-1155.

738   39.   Timcenko, M., et al., *Structure and autoregulation of a P4-ATPase lipid flippase.* Nature, 2019. **571**(7765): p. 366-370.

740   40.   Mi, W., et al., *Structural basis of MsbA-mediated lipopolysaccharide transport.* Nature, 2017. **549**(7671): p. 233-237.

742   41.   Menon, I., et al., *Opsin is a phospholipid flippase.* Curr Biol, 2011. **21**(2): p. 149-53.

743   42.   Pomorski, T. and A.K. Menon, *Lipid flippases and their biological functions.* Cell Mol Life Sci, 2006. **63**(24): p. 2908-21.

745   43.   Olsen, J.A., et al., *Structure of the human lipid exporter ABCB4 in a lipid environment.* Nat Struct Mol Biol, 2020. **27**(1): p. 62-70.

747   44.   Kim, Y. and J. Chen, *Molecular structure of human P-glycoprotein in the ATP-bound, outward-facing conformation.* Science, 2018. **359**(6378): p. 915-919.

749   45.   Perez, C., et al., *Structure of Outward-Facing PglK and Molecular Dynamics of Lipid-Linked Oligosaccharide Recognition and Translocation.* Structure, 2019. **27**(4): p. 669-678.e5.

751   46.   Timcenko, M., et al., *Structural Basis of Substrate-Independent Phosphorylation in a P4-ATPase Lipid Flippase.* J Mol Biol, 2021: p. 167062.

753   47.   Radestock, S. and L.R. Forrest, *The alternating-access mechanism of MFS transporters arises from inverted-topology repeats.* J Mol Biol, 2011. **407**(5): p. 698-715.

755   48.   Basilio, D., et al., *Conformational changes required for H(+)/Cl(-) exchange mediated by a CLC transporter.* Nat Struct Mol Biol, 2014. **21**(5): p. 456-63.

757   49.   Bi, Y., et al., *Architecture of a channel-forming O-antigen polysaccharide ABC transporter.* Nature, 2018. **553**(7688): p. 361-365.

759   50.   Koch, H.U., R. Haas, and W. Fischer, *The role of lipoteichoic acid biosynthesis in membrane lipid metabolism of growing Staphylococcus aureus.* Eur J Biochem, 1984. **138**(2): p. 357-63.

761   51.   Jardetzky, O., *Simple allosteric model for membrane pumps.* Nature, 1966. **211**(5052): p. 969-70.

763   52.   Zhang, B. and C. Perez, *Stabilization and Crystallization of a Membrane Protein Involved in Lipid Transport.* Methods Mol Biol, 2020. **2127**: p. 283-292.

765   53.   Jorasch, P., et al., *A UDP glucosyltransferase from Bacillus subtilis successively transfers up to four glucose residues to 1,2-diacylglycerol: expression of ypfP in Escherichia coli and structural analysis of its reaction products.* Mol Microbiol, 1998. **29**(2): p. 419-30.

768   54.   Kiriukhin, M.Y., et al., *Biosynthesis of the glycolipid anchor in lipoteichoic acid of Staphylococcus aureus RN4220: Role of YpfP, the diglucosyldiacylglycerol synthase.* Journal of Bacteriology, 2001. **183**(11): p. 3506-3514.

771   55.   Peterson, A.C., et al., *Parallel reaction monitoring for high resolution and high mass accuracy quantitative, targeted proteomics.* Mol Cell Proteomics, 2012. **11**(11): p. 1475-88.

773   56.   Ahrne, E., et al., *Evaluation and Improvement of Quantification Accuracy in Isobaric Mass Tag-Based Protein Quantification Experiments.* J Proteome Res, 2016. **15**(8): p. 2537-47.

775   57.   Nesvizhskii, A.I., et al., *A statistical model for identifying proteins by tandem mass spectrometry.* Anal Chem, 2003. **75**(17): p. 4646-58.

777   58.   Trott, O. and A.J. Olson, *AutoDock Vina: improving the speed and accuracy of docking with a new scoring function, efficient optimization, and multithreading.* J Comput Chem, 2010. **31**(2): p. 455-61.

780   59.   Adams, P.D., et al., *PHENIX: a comprehensive Python-based system for macromolecular*
781   *structure solution.* Acta Crystallogr D Biol Crystallogr, 2010. **66**(Pt 2): p. 213-21.
782   60.   Heckman, K.L. and L.R. Pease, *Gene splicing and mutagenesis by PCR-driven overlap extension.*
783   Nat Protoc, 2007. **2**(4): p. 924-32.
784   61.   Monk, I.R., et al., *Complete Bypass of Restriction Systems for Major Staphylococcus aureus*
785   *Lineages.* mBio, 2015. **6**(3): p. e00308-15.
786   62.   Chen, V.B., et al., *MolProbity: all-atom structure validation for macromolecular crystallography.*
787   Acta Crystallogr D Biol Crystallogr, 2010. **66**(Pt 1): p. 12-21.
788   63.   Krivov, G.G., M.V. Shapovalov, and R.L. Dunbrack, Jr., *Improved prediction of protein side-chain*
789   *conformations with SCWRL4.* Proteins, 2009. **77**(4): p. 778-95.
790   64.   Abraham, M.J., et al., *GROMACS: High performance molecular simulations through multi-level*
791   *parallelism from laptops to supercomputers.* SoftwareX, 2015. **1-2**: p. 19-25.
792   65.   Best, R.B., et al., *Optimization of the Additive CHARMM All-Atom Protein Force Field Targeting*
793   *Improved Sampling of the Backbone ϕ, ψ and Side-Chain $\chi1$ and $\chi2$ Dihedral Angles.* Journal of Chemical
794   Theory and Computation, 2012. **8**(9): p. 3257-3273.
795   66.   Jorgensen, W.L., et al., *Comparison of simple potential functions for simulating liquid water.*
796   The Journal of Chemical Physics, 1983. **79**(2): p. 926-935.
797   67.   Klauda, J.B., et al., *Update of the CHARMM All-Atom Additive Force Field for Lipids: Validation*
798   *on Six Lipid Types.* The Journal of Physical Chemistry B, 2010. **114**(23): p. 7830-7843.
799   68.   Darden, T., D. York, and L. Pedersen, *Particle mesh Ewald: An N·log(N) method for Ewald sums*
800   *in large systems.* The Journal of Chemical Physics, 1993. **98**(12): p. 10089-10092.
801   69.   Hess, B., et al., *LINCS: A linear constraint solver for molecular simulations.* Journal of
802   Computational Chemistry, 1997. **18**(12): p. 1463-1472.
803   70.   Berendsen, H.J.C., et al., *Molecular dynamics with coupling to an external bath.* The Journal of
804   Chemical Physics, 1984. **81**(8): p. 3684-3690.
805   71.   Hoover, W.G., *Canonical dynamics: Equilibrium phase-space distributions.* Phys Rev A Gen Phys,
806   1985. **31**(3): p. 1695-1697.
807   72.   Parrinello, M. and A. Rahman, *Polymorphic transitions in single crystals: A new molecular*
808   *dynamics method.* Journal of Applied Physics, 1981. **52**(12): p. 7182-7190.
809   73.   Humphrey, W., A. Dalke, and K. Schulten, *VMD: Visual molecular dynamics.* Journal of
810   Molecular Graphics, 1996. **14**(1): p. 33-38.
811   74.   Gowers, R., et al., *MDAnalysis: A Python Package for the Rapid Analysis of Molecular Dynamics*
812   *Simulations*. 2016. 98-105.
813   75.   Michaud-Agrawal, N., et al., *MDAnalysis: A toolkit for the analysis of molecular dynamics*
814   *simulations.* Journal of Computational Chemistry, 2011. **32**(10): p. 2319-2327.
815   76.   Wu, E.L., et al., *CHARMM-GUI Membrane Builder toward realistic biological membrane*
816   *simulations.* J Comput Chem, 2014. **35**(27): p. 1997-2004.
817
818
819
820
821
822
823
824
825

826

Acknowledgments

835

Author Contributions

E.L. performed *in vitro* and *in vivo* biochemical characterization of LtaA and variants. A.R.M. performed computational analysis. C.P. supervised the biochemical analysis. G.H. supervised computational analysis. A.S. and E.L. performed mass spectrometry analysis. E.L., A.R.M, and C.P analyzed the computational, structural and functional data. C.P. conceived and directed the project. All authors contributed to manuscript writing and revision.

842

Author Information

Competing interests: None declared.

845

846

847

848

849

850

851

852

853

854

855

856

857

858

859 **Figures and Figure legends**
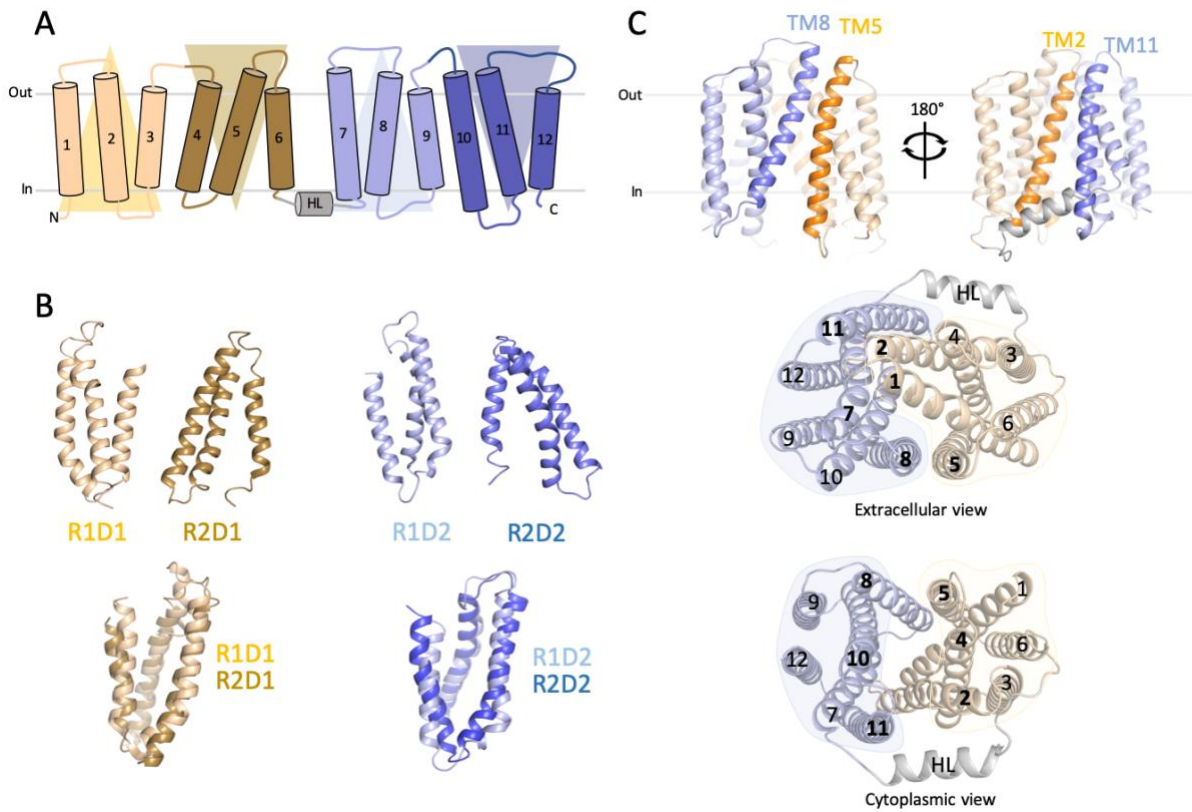
860

861 **Figure 1. 'Repeat swap' modeling of inward-facing LtaA. A**. Topology representation of LtaA.

862 Domain-1 (N-terminal) and domain-2 (C-terminal) are shown in light orange and light blue,

863 respectively. **B**. Individual repeat domains as observed in outward-facing LtaA (PDB ID 6S7V),

864 and superposition of inverted repeats (r.m.s.d. = 2.5 Å and 3.0 Å for aligned Cα atoms of

865 R1D1/R2D1 and R1D2/R2D2, respectively). R1D1 and R2D1 indicate the first and second

866 repeats in the N-terminal domain, respectively, whereas R1D2 and R2D2 indicate the first and

867 second repeat in the C-terminal domain, respectively. Colors are according to panel **A**. **C**. Side-

868 views of inward-facing LtaA model showing TM helices that line the lateral openings.

869 Extracellular and cytoplasmic views are also shown.

870

871

872

873

874

875
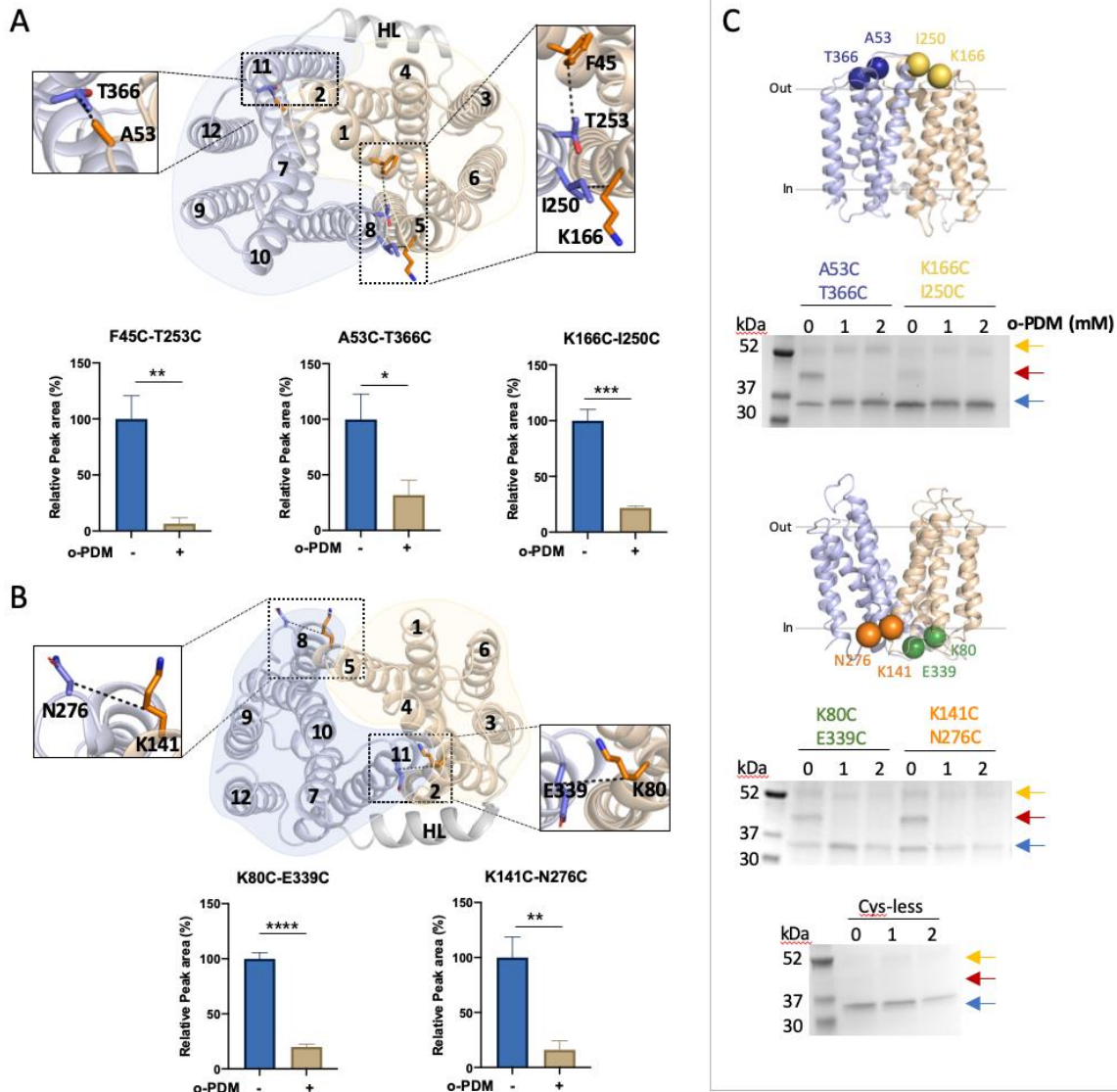
Figure 2. LtaA adopts inward- and outward-facing states. Selected residues for cross-linking of LtaA in inward-facing conformation (**A**) and outward-facing conformation (**B**). N-terminal and C-terminal domains are shown in light orange and light blue, respectively. The relative abundance of cysteine containing peptides in absence (-) or presence (+) of o-PDM is shown in histograms. Collision-induced dissociation (CID) spectrum of cysteine containing peptides and elution profiles of peptide fragments are shown in supplementary figure 3. Error bars indicate standard deviation (s.d.), n≥3. *: P≤0.05, **: P≤0.01, ***: P≤0.001, ****: P≤0.0001. **C**. Cross-linking analysis of LtaA in proteoliposomes. Positions of selected cysteine pairs at the extracellular and cytoplasmic regions of LtaA are shown as spheres. SDS-PAGE show band shifts of samples treated with mPEG5K after irreversible cross-link with o-PDM. Separated species are indicated with arrows. Blue arrow: non-PEGylated LtaA; red arrow: PEGylated LtaA; orange arrow: LtaA dimer.
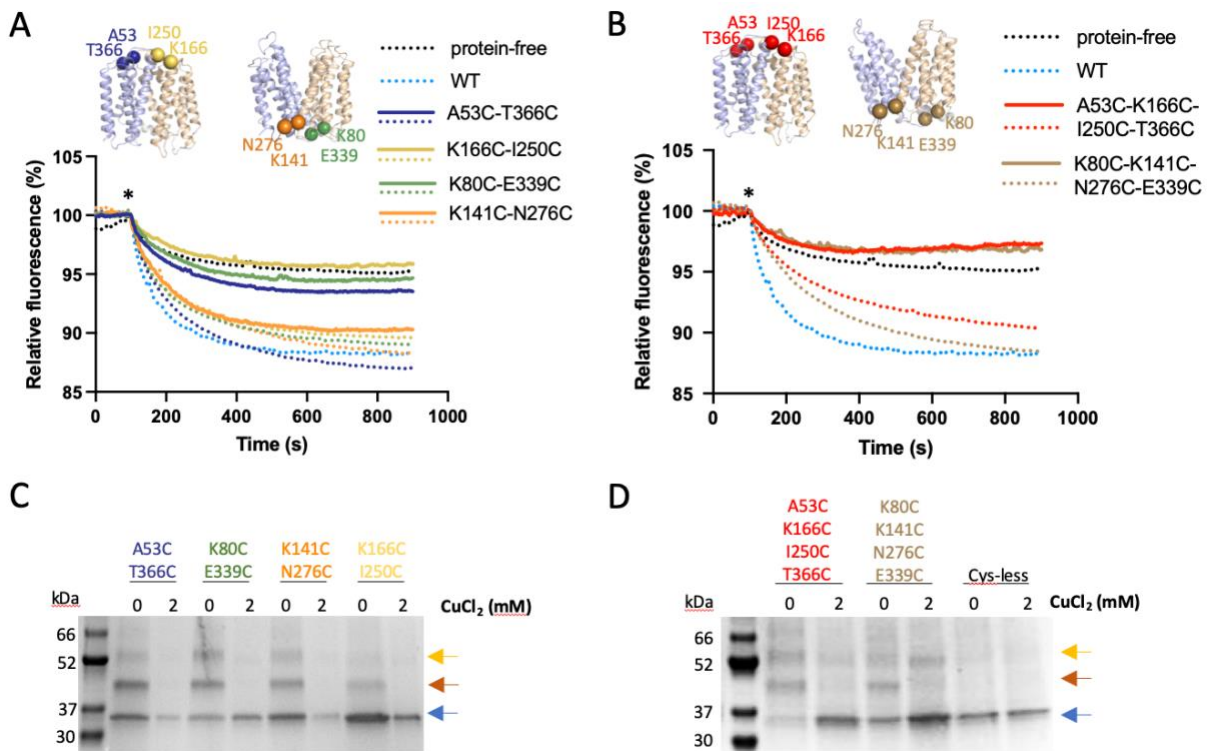
Figure 3. **Cycling through outward- and inward-facing conformations is essential for LtaA activity. A**,**B**. Proton-transport activity of LtaA and variants after chemical crosslinking with CuCl$_2$ (solid lines) or in absence of cross-linking treatment (dotted lines) (n≥3). Proteoliposomes and protein-free liposomes containing 100 mM KCl were diluted in buffer containing 10 mM KCl, 90 mM NaCl and ACMA. H$^+$ influx was initiated by establishing a membrane potential upon addition of the potassium ionophore valinomycin (asterisk). **C.D**. SDS-PAGE shows band shifts of samples treated with mPEG5K after cross-link with CuCl$_2$. Separated species are indicated with arrows. Blue arrow: non-PEGylated LtaA; red arrow: PEGylated LtaA; orange arrow: LtaA dimer.
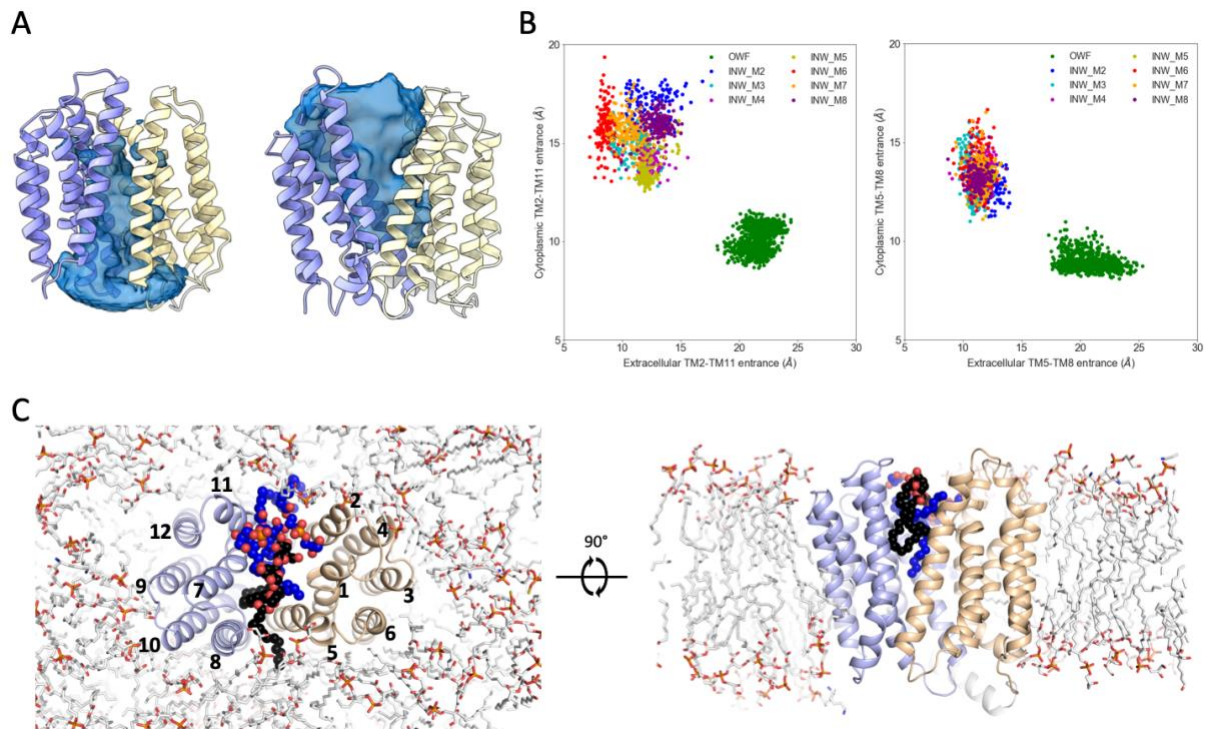
Figure 4. **LtaA displays asymmetric opening of cavities and lateral 'gates'. A**. Representative view of solvent exposed cavity of inward-facing and outward-facing LtaA as observed during MD simulations. **B**. Analysis of distances between TM helices lining the cytoplasmic and extracellular lateral openings of outward-facing and inward-facing models. The center of masses of the Cα atoms of extracellular residues 52-57 (TM2), 163-167 (TM5), 250-255 (TM8), 364-367 (TM11), and of cytoplasmic residues 77-81 (TM2), 139-143 (TM5), 273-276 (TM8), 341-344 (TM11), were used for the calculation of inter-TM distances. **C**. Intrusion of gentiobiosyl-diacylglycerol (black spheres) and POPG (blue spheres) molecules in the extracellular cavity of LtaA during simulations. N-terminal and C-terminal domains are shown in light orange and light blue, respectively.

29

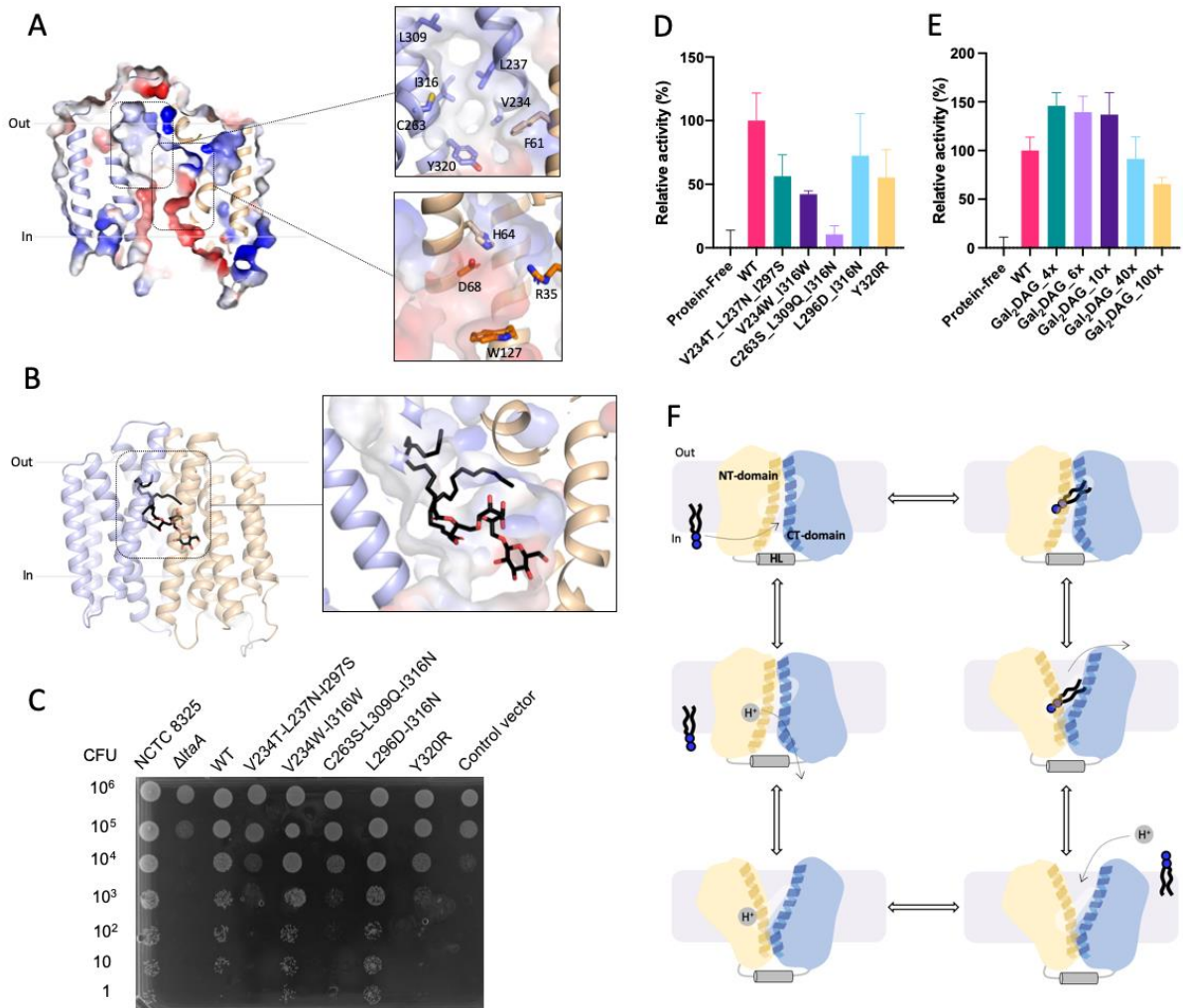**Figure 5**. **Hydrophilic and hydrophobic cavities participate in 'trap-and-flip' of lipids. A**. Vacuum electrostatic surface representation of inward-facing model of LtaA. Residues forming the hydrophobic and hydrophilic pockets are shown. **B**. A model of a glycolipid molecule docked into the amphipathic cavity of LtaA. The lipid tail length corresponds to C16 chains. N-terminal and C-terminal domains are shown in light orange and light blue, respectively. **C**. *S. aureus* cell growth on LB agar plates containing 0.1 mM IPTG, buffered at pH 6.4. The *ΔltaA* mutant is complemented with pLOW vector carrying a *ltaA*-WT gene or the annotated point mutations; Control vector indicates the pLOW vector carrying an unrelated gene (dCas9). **D.** Mutagenesis analysis of the hydrophobic pocket. Relative flipping activity of LtaA-WT and variants. Error bars show s.d. of technical replicates, n≥3. **E**. Headgroup selectivity analysis. Relative flipping activity of LtaA in the presence of different concentrations of digalactosyl-diacylglycerol (Gal$_2$DAG). Molar excess of Gal$_2$DAG over Glc$_2$-DAG-NBD is indicated. Error bars show s.d. of technical replicates, n≥3. **F**. Proposed mechanism of LtaA

30

942   catalyzed glycolipid transport. Schematic of conformational states throughout LtaA transport

943   cycle.